ADVANCED MATERIALS TECHNOLOGIES
www.advmattechnol.de

Time- and Frequency-Domain THz Imaging for the Characterization of Subwavelength Tags in Anticounterfeiting Devices

Tiziana Ritacco, Dimitrios C. Zografopoulos, Silvia Tofani, Romeo Beccherelli, and Walter Fuscaldo**

Hidden tags are robust and efficient security systems for protecting assets but their identification requires nondestructive techniques. Here, a contactless, efficient, terahertz (THz) investigation protocol based on the electromagnetic interaction between THz radiation and materials with subwavelength features is presented. On top of an opaque, lossy dielectric substrate a metal "open tag" is patterned as reference. This contains features that are visible to the naked eye, but subwavelength in the THz range. An identical dielectric substrate is then used to cover the metallic pattern and fabricate a "hidden tag." Both tags are then scanned using a THz time-domain spectroscope (TDS). The collected spectra are used to evaluate different metrics, which provide valuable pixel-specific information for sample imaging. While the most common imaging techniques are demonstrated to be unsuitable for decoding hidden tags, a thorough study of the THz response allows to determine the best conditions for creating high-resolution images in both time- and frequency-domain. Effective metrics are obtained by isolating the peaks of the signal reflected from the tag or the substrates, or by suitably considering the interaction between the two signals. The proposed method provides a rigorous protocol for the THz imaging of hidden logos in multilayer systems, which can serve as anticounterfeiting tags.

1. Introduction

Driven by the escalating presence of counterfeit products across industries at multiple levels, which poses both economic and safety risks, recent years have witnessed a significant increase in the demand for anticounterfeiting devices and technologies to decode authentication tags.[1–5] One of the approaches to address this issue has been the additive manufacturing of optical tags, usually made in materials doped with dyes,[6–8] quantum dots,[9–12] nanoparticles[13,14] or liquid crystals.[15–18] While these strategies are often difficult to fabricate and expensive, they endow the tag with an optical fingerprint, that goes beyond its morphology.[19–21] However, many of these tags have a major shortcoming: in order to be read, they must be placed on the surface of the device, thus making them susceptible to damage, destruction, and, in some cases, easy falsification.

A hidden tag, incorporated inside a device, can provide a more robust solution for product authentication and can hardly be recognized by counterfeiters. Conversely, it does not provide a straightforward way to decode the product without damaging it.

Among the different techniques proposed so far to circumvent this issue, terahertz time-domain spectroscopy (THz-TDS) is the most suitable one to perform nondestructive analysis on multilayer complex devices, thanks to the high penetrating capability of the THz radiation into nonconductive materials and nonpolar molecules, with respect to the visible light, while featuring a nonionizing character as opposed to X-ray technologies.[22–25]

Thanks to these properties, in the last decade, THz-TDS imaging has been exploited in the field of medical imaging,[26–29] cultural heritage,[30–35] quality control,[36–40] and, more recently, in anticounterfeiting applications.[41–44] Usually, an infrared femtosecond laser is connected to a photoconductive antenna, generating a THz pulse. The signal propagates through the sample and is collected by a second antenna and detected. However, when a metal-dielectric multilayered electrically thick device is analyzed, measurements in transmission mode can fail to accurately detect the sample features. While the radiation can penetrate most dielectric materials, it is strongly reflected by metallic parts, making this kind of analysis unsuitable for many devices, like electronic chips or paintings based on metallic inks. On the other hand, such

T. Ritacco, D. C. Zografopoulos, S. Tofani, R. Beccherelli, W. Fuscaldo
Istituto per la Microelettronica e Microsistemi
Consiglio Nazionale delle Ricerche
Rome 00133, Italy
E-mail: tiziana.ritacco@cnr.it; walter.fuscaldo@cnr.it

The ORCID identification number(s) for the author(s) of this article can be found under https://doi.org/10.1002/admt.202401799

DOI: 10.1002/admt.202401799

information can be readily obtained through THz-TDS in reflection mode.

When operating in reflection mode, the sample is scanned in both x and y directions and the time traces of the reflected signal are collected from each point. Different THz images can be obtained by assigning to each pixel (i.e., each measured point) a "time-domain" metric, such as the maximum value of the first peak, the intensity at a specific time, the peak-to-peak distance, the energy, or the average intensity.[45–47] By Fourier-transforming the time traces, one can also assign to each pixel a "frequency-domain" metric, such as the amplitude of the reflectance spectrum at a specific frequency.

While time-domain metrics provide information about morphology and stratification (i.e., each layer interacts with the THz signal at specific time intervals), frequency-domain metrics help in recognizing the sample composition, since many materials have specific spectral THz signatures.[48–52] However, these analyses may not be enough to recognize the characteristics of multilayered devices, especially when the relevant information is embedded in intermediate layers, as with hidden tags, and/or when materials with no clear THz fingerprints are used (e.g., common metals and polymers). These considerations hold even more true when metallic patterns exhibit a subwavelength character as in the cases here investigated.

In multilayered samples, multiple reflections occur at the same pixel. Radiation going through the different layers may be partially or completely reflected at the interfaces due to mismatches in refractive indices. As a result, multiple echoes are collected at different times, depending on the optical path length of the THz wave that undergoes through each layer. Since information from intermediate layers can be obscured by the responses of other layers, different types of imaging techniques should be considered to decode features at different depths, each designed to improve the contrast between signals from specific layers and the overall device. For instance, in cultural heritage,[46] THz techniques were used for the identification of features located on different levels in a stratified portrait. This task requires multiple metrics, obtained by analyzing different segments of the raw time traces to isolate information from each layer. A similar approach is necessary but not sufficient to decipher hidden tags. Moreover, even when some metrics (i.e., the signal amplitude at specific frequency values) may decode hidden tags, this approach does not always consider the electromagnetic interaction of THz waves in multilayered media, providing only partial information and making it hard to predict all the tag features.

Our objective of producing physics-based metrics—both in time and frequency domain—focuses on the electromagnetic interaction between the THz signal and each layer. We show how this analysis allows both to significantly improve the image contrast in the context of anticounterfeiting and to predict the unfalsifiable tag THz signature. To demonstrate the effectiveness of the proposed technique, we have designed a hidden tag featuring a patterned copper logo concealed between two ceramic substrates, with the bottom substrate back-covered by a copper layer. The materials and the geometry are specifically chosen to exploit the differences in the signal behavior between metallic and dielectric layers and confer a specific signature on the tag. Remarkably, it will be shown that the subwavelength character of the details of the logo plays a key role in determining the temporal and spectral signature of the hidden tag; an aspect so far overlooked. The analysis presented in this work can be applied to any stratified tag, provided that the initial layer is not highly reflective and allows the penetration of THz radiation.

Common dielectric materials suitable for product tagging, such as teflon, polyethylene, cyclic olefin polymers and ceramics are most suitable for the external layer, since the thickness, opaqueness, and reflectivity prevent both morphological and visible-optical techniques from detecting the logo hidden within the device. Comparing the THz imaging of the opened and closed logo demonstrates how most commonly used imaging techniques,[30–33,37,38] fail to decode the tag. Conversely, we show here that our proposed strategies are efficient tools for the correct identification of the logo (or the tag).

In the following, we describe in detail the physics underlying the proposed imaging techniques and experimentally demonstrate their effectiveness in a practical case study.

2. Hidden Tag Fabrication

Figure 1 illustrates the tag fabrication scheme. Two 30.00 × 30.00 × 0.64 mm^3 opaque ceramic, quasi-flat substrates (Rogers RO3006), covered by a 35-µm electrodeposited copper film on both sides, are used. Their dielectric properties in the THz range have been already characterized in ref. [53], revealing a refractive index and loss tangent that vary from 2.66 to 2.63 and from 0.02 to 0.11, respectively, in the 0.3–1.5 THz bandwidth. These values compare to 2.4 and 0.002, respectively at 10 GHz, as per the manufacturer data sheet. Thus, losses in the THz regime are one order of magnitude larger. We will show in the following, that these losses are advantageously used.

The substrates are cleaned in an ultrasonic bath, first in acetone, followed by isopropyl alcohol, and finally in deionized water, for a total of 15 min. They are then dried with nitrogen at room temperature. A 1.3-µm thick film of the positive photoresist Microposit S1813 by Rohm is spin-coated (10 s at 500 rpm, 60 s at 4000 rpm) on one side of both substrates and prebaked at 115 °C per 90 s.

The "Safe" logo is printed with black ink on a translucent foil, which is then put in contact with one substrate under vacuum conditions. Using a 390 nm UV lamp at 100 mJ with an exposure rate of 5 mJ s^{-1}, all the photoresist except for the logo is exposed. The photoresist is then developed in a bath of MF319 by Rohm for 45 s and rinsed with water for 10 s to cleanse all the exposed material.

Next, the two substrates are immersed in a copper wet-etching solution (100 mL H_2O, 60 mL HCl, 20 mL H_2O_2) to remove the copper films not covered by the photoresist. After etching, the substrates are rinsed with deionized water. In this way, one of the substrates remains completely metalized on one side, while the second substrate presents only the "Safe" copper logo patterned on one of its surfaces. All the remaining photoresist is removed using acetone, and both substrates are then cleaned with isopropyl alcohol followed by deionized water, before being dried with nitrogen. The substrate presenting the logo (i.e., the open tag) is fully characterized by THz-TDS. The two sides are then assembled with the logo hidden inside and glued on all sides with the Norland Optical Adhesive 68 epoxy resin, which is then fully UV-cured at 5 J under vacuum conditions.

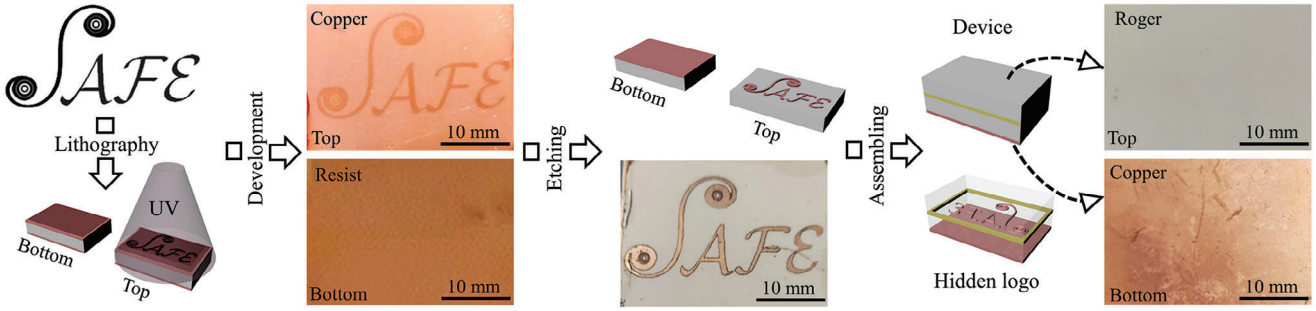

Figure 1. Hidden tag fabrication processes. The "Safe" logo is printed with a black ink on a translucent foil, that is used as a mask in the photolithographic process. After development, the two substrates are etched and cleaned. The copper on the top substrate is completely removed, except for the patterned logo, while the bottom substrate is still metalized on one side. The two ceramic layers are assembled with the logo hidden in their interior interface.

The final device is a multilayered structure with a Rogers substrate on top, the "Safe" logo at the mid-interface, a second Rogers substrate and finally the copper film. We note here that the letters in the "Safe" logo have features in the order of fractions of millimeters. Since the THz beam is typically larger than the wavelength—which ranges from 0.2 to 1 mm in the considered frequency range—THz radiation is not entirely reflected by the metallic parts that mostly show a subwavelength character. This aspect will have important consequences in the temporal fingerprint of the hidden tag as we will comment in the next Section.

Moreover, due to the high opacity and thickness of the Rogers substrates, commonly used investigation techniques such as profilometry, atomic force microscopy, near-infrared (NIR) or visible light imaging, and electron scanning microscopy are unsuitable for identifying the logo. While X-beam tomography could potentially succeed in this task, it may pose risks to both the device and the operator. Therefore, THz investigation proves to be the most suitable method for examining this type of device.

3. Time-Domain Analysis

The time traces are acquired by using the TeraFlash Pro (Toptica AG Photonics[54]) THz-TDS imaging system in reflection mode. The sample is placed on an aluminum plate and the THz beam is focused on it and collected by using two pairs of parabolic mirrors, with an angle of incidence $\theta_i = 8°$ with respect to the normal direction. The setup is configured to record THz signals over a time window of 200 ps, so as to collect higher-order echoes due to multiple bounces experienced by the THz wave interacting with the multiple layers of the device.

Before assembling the tag, a 2.8×2.8 cm^2 area of the substrate with the patterned logo is scanned in both the x and y directions, with a 0.2 mm step size. The recorded time signal at each point results from the averaging of five (single-shot) measurements. The same analysis is then repeated for the assembled tag. As shown in **Figure** 2a,b, the THz signal is reflected differently by the open and the closed tags. In the first case, the signal impinging

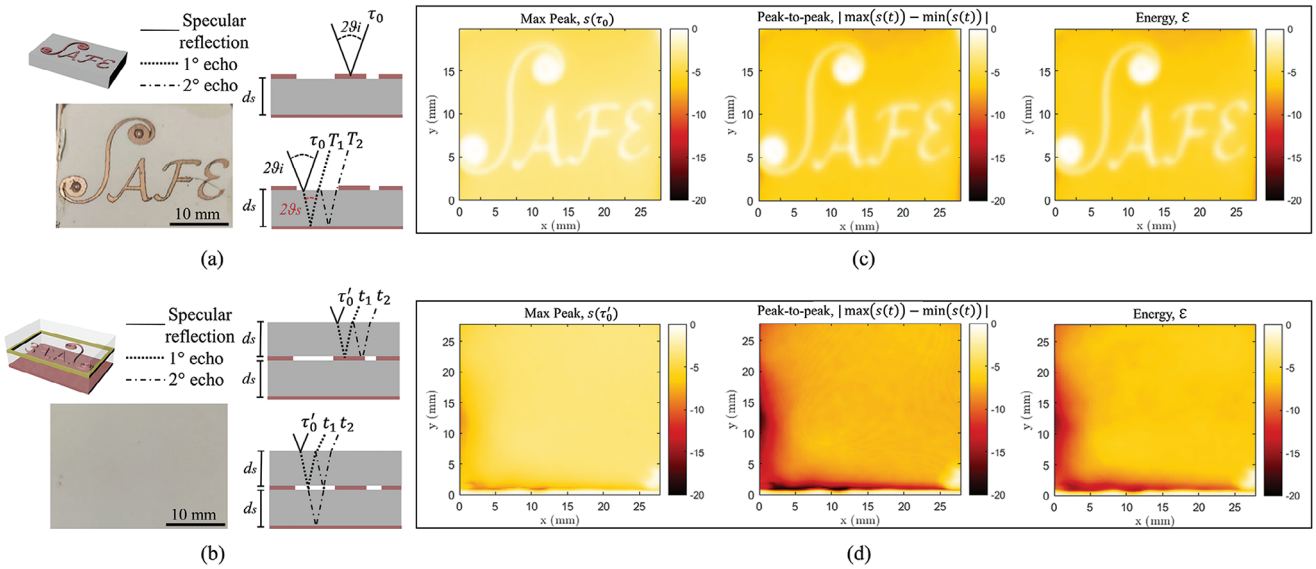

Figure 2. Schematic showing the THz radiation-material interaction on a) the open and b) the assembled tag. c–d) Images based on the highest amplitude value, the peak-to-peak intensity, and the energy integrated on all the time range, obtained for the a) and b) cases, respectively. The highly conducting "Safe" tag is clearly visible in the open device while is not decoded in the closed device. Color bars are reported in dB.

directly on the metal logo is completely reflected and is acquired at time

$$\tau_0 = 2d_0/(c_0 \cos\theta_i) \quad (1)$$

where d_0 is the path length between one antenna and the open tag, and c_0 the speed of light in a vacuum. We refer to this signal as the "zeroth-order echo." On the other hand, the nonpatterned surface of the dielectric ceramic only partially reflects the signal (specular reflection), due to the refractive index mismatch, with the remaining portion being transmitted through the substrate and then reflected from the last metallic layer, which helps in avoiding an air gap between the tag and the sample holder. This results in multiple echoes, as each beam follows a distinct optical path. The path length is increased by

$$d_N = 2Nn_s d_s/\cos\theta_s \quad (2)$$

where N is the number of echoes, d_s the thickness of the substrate, $\theta_s = \arcsin\left(\sin\theta_i/n_s\right)$ and $n_s = 2.64 \pm 0.01$ the Rogers 3006 average refractive index calculated in the 0.3–1.5 THz range,[53] respectively. Therefore, the "higher-order echoes" from the open tag are registered at $T_N = \tau_0 + \Delta\tau_N$ with optical delays (from the zeroth-order echo at τ_0):

$$\Delta\tau_N = d_N/c_0 = 2Nn_s d_s/(c_0 \cos\theta_s) \quad (3)$$

For $N = 1$, $\Delta\tau_N \simeq 11$ ps.

The hidden tag, being a multilayered structure with alternating metallic and dielectric layers (Figure 2c), presents a more complex optical geometry. The specular reflection occurs on the uniform ceramic layer at

$$\tau_0' = 2d_0'/(c_0 \cos\theta_i) \quad (4)$$

where d_0' considerably differs from d_0 (and in turn τ_0' from τ_0) because of the different thickness of the tags (the hidden tag thickness is almost twice the open tag). As opposed to the open tag, here only the portion of the signal that is transmitted inside the device interacts with the logo. This transmitted signal is further split into several rays that follow different paths depending on whether they fall inside or outside the logo area. In particular, inside the "Safe" region, the optical path is similar to the one observed outside the logo in the open tag, with each beam being registered with the optical delays $\Delta\tau_N$, meaning each 11 ps after the specular reflection. (We recall here that the logo in the hidden tag is sandwiched between two substrates identical to the one used for the open tag.) Outside the patterned area, the signal goes through the first Rogers substrate, an air gap, and the second substrate before being reflected by the copper layer at the bottom.

The presence of an air gap is unavoidable due to differences in the local thickness of the two substrates and the assembling procedure. The thickness of this gap ranges from almost 0 μm (at the side of the substrate, far from the logo area) to a 120 μm (close to the logo area where a minimum gap of 35 μm is due to the copper layer), which induces a non-negligible/measurable effect in the propagation of the THz wave.

Therefore, the first ray passing through the initial dielectric layer is split into two signals with optical delays $\Delta\tau_N$ (reflection at the first ceramic-air interface) and $\Delta\tau_N + \Delta\tau_{gap}$ (reflection at the second air-ceramic interface), where $\Delta\tau_{gap} = 2d_{gap}/(c_0 \cos\theta_i)$ is the delay due to the air gap. The temporal separation between these two signals can be rather narrow in areas far from the logo where the gap is small (we remark that dimensions lower than 7 μm are below the system temporal resolution, namely, 50 fs). We will see next that the contributions from these signals are rarely resolved by the system and rather merge into a single echo.

The remaining part of the signal passes through the second layer and is eventually reflected by the metalized surface, following a similar pattern in reverse sense. The higher-order echoes from the hidden tag are registered with optical delays:

$$\Delta\tau_N' = d_N/c_0 = 2\Delta\tau_N + N\Delta\tau_{gap} \quad (5)$$

Since $\Delta\tau_{gap}$ ranges from 0 fs to hundreds of femtoseconds (as can be readily obtained from a straightforward application of Equation (3) to air gaps as large as 120 μ m), the first echo from the entire device is thus registered almost simultaneously with the second echo from the logo, i.e., with an optical delay $\Delta\tau_{1,dev}' = 2\Delta\tau_1 + \Delta\tau_{gap} = \Delta\tau_2 \simeq 22$ ps.

The results presented so far indicate that, for the open tag, images generated by assigning each pixel the signal intensity $s(t)$ registered at time values $t \geqslant \tau_0$ always reveal the logo. In fact, at $t = \tau_0$ the signal reflected from "Safe" is registered, at $t > \tau_0$ the signal reflected outside "Safe" is registered, but in all cases, the imaging contrast is always sufficient to recognize the logo. Vice versa, for hidden tags, this type of metrics only reveals the tag at certain times $t_N = \tau_0' + \Delta\tau_N'$ and, for even values of N, the detected signal is a combination of the echoes from the logo and the two substrates. In addition, these metrics primarily provide information about the morphology of the device and are highly sensitive to its flatness. Any surface roughness locally alters both the time delay of the specular reflection and the optical path, potentially leading to unclear imaging contrast or false features.

For these reasons, other information must be considered for the accurate imaging of multilayered devices. Most common imaging techniques typically assign to each pixel the maximum of the amplitude signal (specular reflection) $s(\tau_0)$, the peak-to-peak intensity $|\max s(t) - \min s(t)|$, and the energy integrated over the entire spectrum $\mathcal{E} = \int_{t_{min}}^{t_{max}} s(t)^2 dt$. In Figure 2c,d, we compare the images obtained for the open and the assembled tags, respectively. In all cases, while the open tag imaging is clear and well-defined, showing all the features of the "Safe" logo, including the "spiral" pattern in the "S", no information is visible for the hidden tag, but for the energy imaging, in which the logo is barely recognizable and its features are not well resolved (Figure 2d, right panel). By using other common metrics, such as the energy of the first peak $\mathcal{E}_{t_1} = \int_{t_1-\Delta t/2}^{t_1+\Delta t/2} s(t)^2 dt$, where t_1 is the time of the first peak maximum and Δt is a 2 ps time window around the peak, the tag is not recognizable as well.

These data demonstrate that most of the signal is specularly reflected at the first air-ceramic interface, which is the main contribution to all these metrics, yet it does not contain any information about the stratification inside the device. The intensity of the residual signal collected from high-order echoes is not sufficient to distinguish it from the noise in the most common metrics, so they fail to decode the hidden tag.

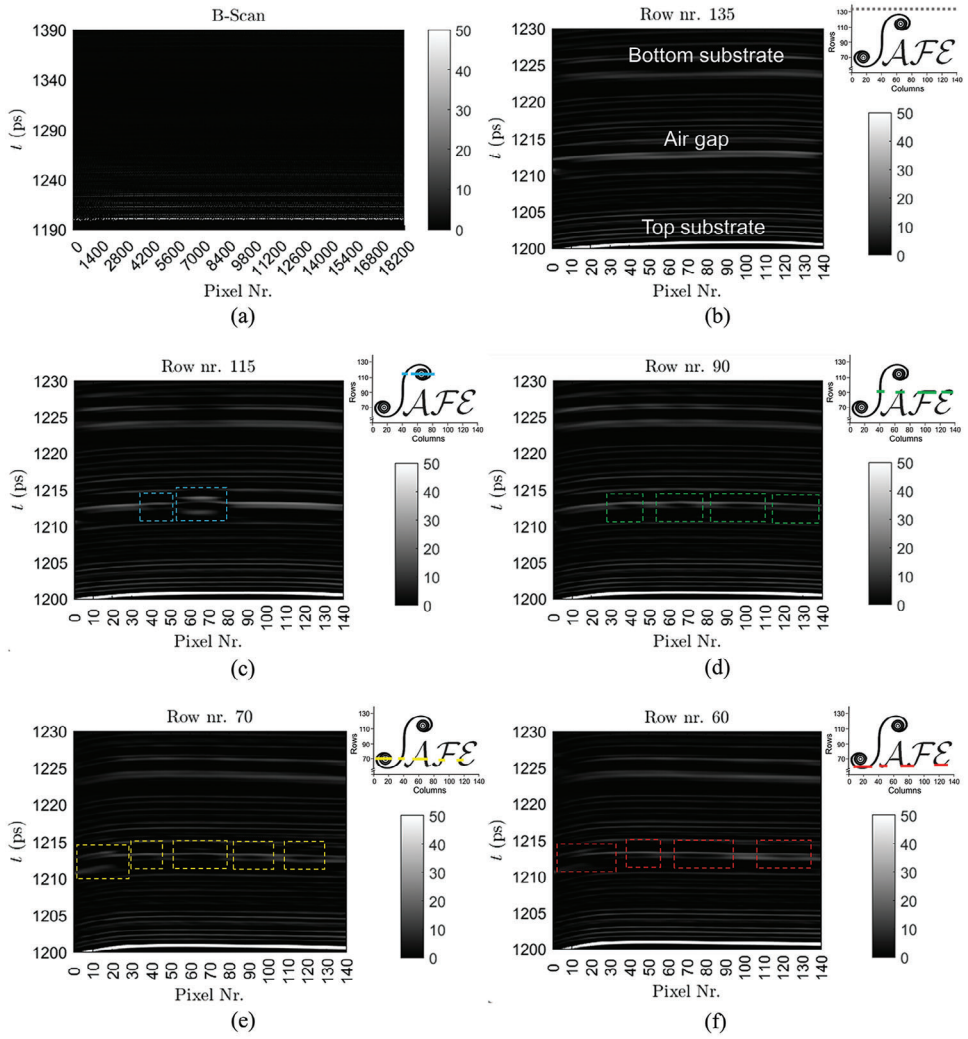

Figure 3. a) Time-domain spectra obtained for each pixel, reported row after row (each row contains 140 pixels of 0.2 × 0.2 mm^2 size). Analysis of the single rows: b) Row nr. 135, outside the logo; c) Row nr. 115, on the upper part of the "S" of "Safe"; d) Row nr. 90, at the logo center, corresponding to the top of most letters; e) Row nr. 70, at the bottom of the "Safe" and the center of other letters; f) Row nr. 60, at the bottom of the logo. The scale bar is in dB.

To correctly identify the tag, a detailed analysis of the time-domain signals acquired for each pixel is mandatory. In the radargram in **Figure** 3a, also known as B-scan, all the time-domain signals for the hidden-tag sample are reported as a reference. Focusing on a single row of the sample that contains no logo features (Figure 3b), the signals clearly reveal the stratification of the various interfaces. This stratification includes the surface of the top substrate, the interface between the two Rogers substrates with the air gap outside of the logo, and the bottom copper layer. In principle, the maximum thickness of the gap d_{gap} can be precisely controlled and minimized (ranging from 0 to 35 µm, namely up to the thickness of the copper layer) by assembling the device under vacuum conditions. On the other hand, some randomness in the spacing, which is known to the manufacturer, increases the security level as it contributes to a unique fingerprint. Hence, we choose to directly assemble the two sides of the device without using spacers to trap an air layer of random thickness for each pixel. In this way, each device has a unique and hard-to-reproduce B-scan, that can be registered by the tag manufacturer and used as a secure key for future authentication.

By analyzing different rows outside the patterned area, we find that, in the time interval 1211–1213 ps, the optical delay between the two air-ceramic interfaces is detected. The delay ranges from 0 fs (at the edges) to 800 fs (in the central area), meaning that d_{gap} varies from 0 to 120 µm across the device. In the areas near the logo (within 2 mm of the latter features), the air gap is more uniform, with optical delays between 560 and 800 fs, corresponding to a d_{gap} of 80 to 120 µm. In this respect, it is worthwhile to note that the differences in the gap size manifest themselves in the B-scan (see the air gap region in Figure 3b) as areas where two distinct, still faint peaks appear (larger gaps) and areas where a merged, reinforced peak appears (smaller gaps), in agreement with the previous discussion.

When the same analysis is performed on rows corresponding to the logo (Figure 3c–f), the first-order echo produced by the metallic "Safe" letters is well distinguishable and occurs at the

predicted optical delay (i.e., 11 ps). It is worthwhile to note that the signal reflected by the first layer is consistently stronger than the one reflected by the metal parts. This effect has a twofold reason: first, the significant step index difference between the air and ceramic leads to a high reflection; second, the loss tangent of the Rogers substrate (viz., $0.02 < \tan\delta < 0.11$ in the 0.3–1.5 THz range[53]), causes non-negligible absorption. We also underline that on large metal areas, the signal would be entirely reflected, making the gap unrecognizable since the logo is located on the back of the first side. However, the wavelength of the considered THz radiation, which ranges from 0.2 to 1 mm, is comparable to the size of the sides and features of the "Safe" metallic letters which range between 0.3 mm (internal circle of the "S" and left side of the "A") and 1.0 mm (external circle of the "S"), causing scattering effects, mainly edge diffraction, and part of the signal still reaches the second surface.

As a result, the echoes in the B-scan are discernible due to the increased separation between the two interfaces, resulting from the scattering effect (dotted squares in Figure 3c–f). This effect is particularly evident in the "spiral" pattern at the edges of the "S." At these wavelengths (Figure 3c,e), the THz wave may diffract in multiple directions at the edges of the metallic pattern, thus enhancing the optical delay between the two interfaces to 2 ps. The second-order echo is expected at 22 ps after the main reflection; however, as shown in Figure 3b, the B-scan analysis demonstrates that even the first echo from the last layer is registered almost simultaneously, since the two ceramic layers have the same thickness. Consequently, while this analysis is sufficient to detect the presence of the logo, we still need the imaging analysis to decode all the information. Figure 3c–f clearly illustrates why common metrics fail to detect the logo: they all include the specular reflection, whose intensity is about four times higher than that of the logo echoes.

We deduce that two strategies are most effective in generating metrics for anticounterfeiting. The first one considers the energy of the reflected signal integrated after a time delay τ_d, in order to exclude the specular reflection. In **Figure** 4a–c, examples of time-domain images generated from the following metrics

$$\mathcal{E}_{\tau_d} = \int_{\tau_0+\tau_d}^{t_{max}} s(t)^2 \mathrm{d}t \tag{6}$$

with τ_d equal to a) 5 ps, b) 10 ps, c) 20 ps, are reported. At the bottom of each figure, the graph displays all the superimposed time signals, with the gray rectangle indicating the time window over which the remaining portion of the signal is integrated. For τ_d = 5 ps, part of the acquired signal still results from the interaction between the THz radiation and the Rogers substrate. As a result, while the logo becomes visible, the imaging contrast is reduced. Vice versa, integrating the energy over the temporal range from τ_d = 10 ps onward (Figure 4b) completely neglects the initial contribution from the first layer, making the logo echo the most prominent signal, thereby maximizing the imaging contrast. When the delay is increased to τ_d = 20 ps, the imaging is influenced by contributions from the second-order echoes from both the logo and the two substrates. Although the tag is still deciphered, the imaging contrast is reduced.

The second strategy is to consider only the energy integrated into the time windows in which the logo echoes are registered, specifically within a Δt = 4 ps window around the t_N values:

$$\mathcal{E}_{t_N} = \int_{t_N-\Delta t/2}^{t_N+\Delta t/2} s(t)^2 \mathrm{d}t \tag{7}$$

In Figure 4d–f, the time-domain images display the energy integrated over the first- (N = 1), second- (N = 2), and third-order (N = 3) echoes, respectively. The integrated part of the spectra is highlighted at the bottom, while the echo behavior is shown at the top. We underline that the time-domain image obtained by the first echo (Figure 4d) is the one with the highest imaging contrast, allowing to resolve the smallest logo features, such as the hole in the "A" and the spiral shape of the "S." As shown in Figure 4e, the second-order echo occurs simultaneously with the first-order reflection from the bottom layer. Therefore, the time-domain image obtained from the second-order echo (Figure 4e) is less resolved, with the logo edges in low contrast with respect to the background. However, in the two holes at the center of the "S," the two signals interact constructively, resulting in more intense energy integration in these pixels. For the third-order echo (Figure 4f), the energy from the background is higher than that from the "Safe" letters, thus while the presence of a metallic logo is still detectable by the color contrast, it is no longer decipherable.

It is also worth noting that, in most of the images in Figure 4, the signal integrated from the logo is less intense than that from the substrates. This contrasts with the open tag, where the signal reflected by the metal parts is consistently stronger than that from the surroundings, thus the logo appears brighter in the images (Figure 4c). The main difference between the imaging obtained from the two devices is due to the presence of the air gap in the closed device. When the signal passes through the first ceramic layer, it is partially transmitted into the air gap, where it can either be transmitted to the second ceramic layer, reflected back by it, or undergo multiple reflections within the air gap. Consequently, a portion of the signal is reflected back into the first ceramic layer and eventually reaches the surface after just a few femtoseconds, depending on the gap thickness, and well within the considered time interval of integration. Therefore, the signal collected from each pixel arises not only from the direct reflection of the THz radiation off the impinged area, but also from the collective contribution of the higher-order echoes occurring in the air gap in nearby areas. Conversely, the signal in the gap that encounters the metal logo cannot be transmitted, but it is completely reflected back within the gap. Thus, in the vicinity of the logo, only the signal reflected directly by the metal is detected, and its intensity is lower than that of the signals registered due to the air gap in the surrounding areas. Only at the third echo (Figure 4e), this effect results negligible.

4. Frequency-Domain Analysis

By Fourier-transforming the time-domain raw spectra, we calculated the frequency-domain response of the device in the 0.5–1.0 THz range, with a frequency resolution of 1 GHz, obtained by zero-padding the 200-ps-long time traces until 1 ns. In this spectral window, the instrument provides maximum signal–to–noise

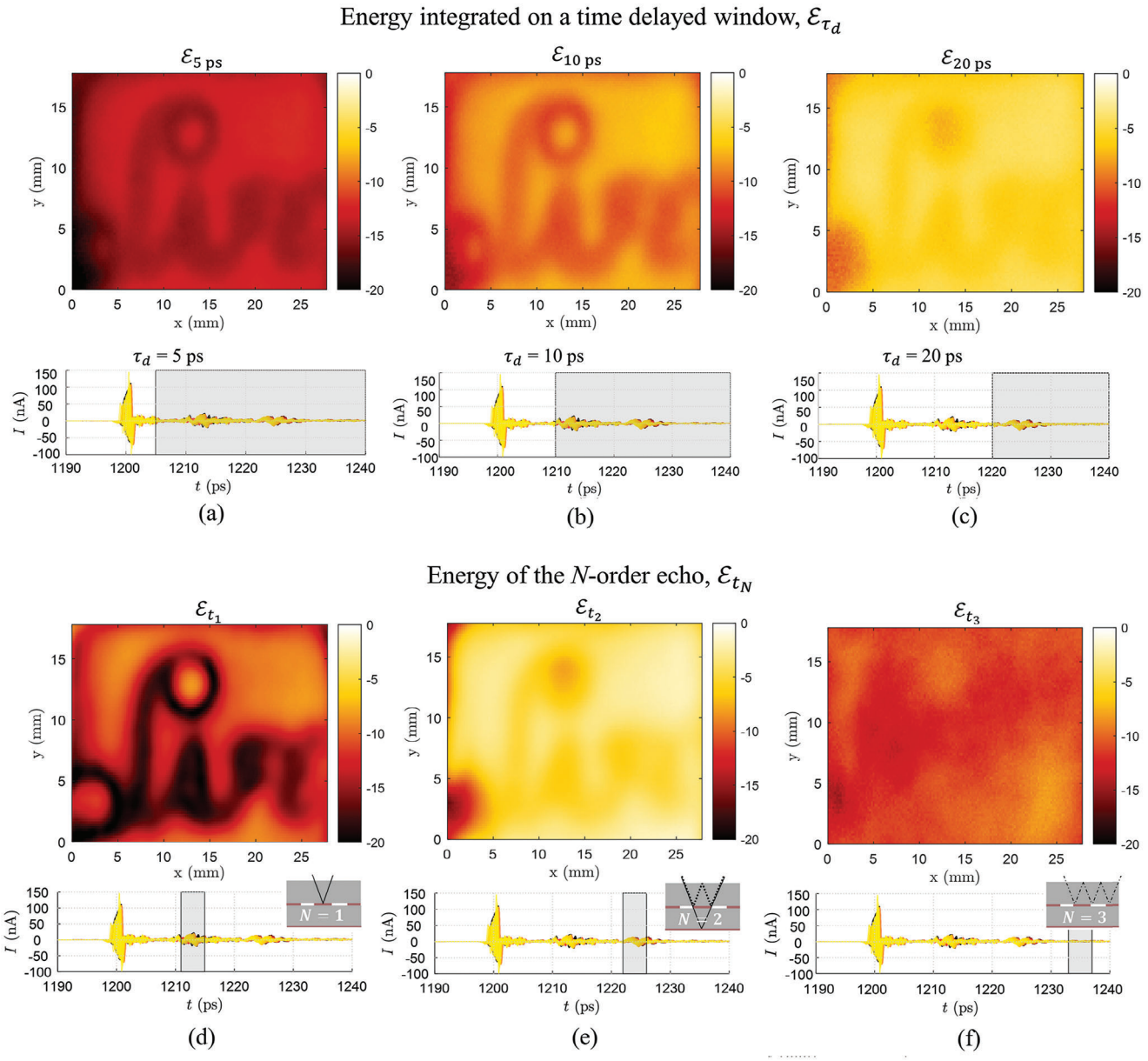

Figure 4. Time-domain images of the hidden tag. For all figures the color bar represents the energy integrated in a window of time delayed of a) 5 ps, b) 10 ps, c) 20 ps or in a window of 4 ps including the d) first, e) second and f) third echoes from the metallic logo. On the bottom of each image, the graph of the superimposed raw time traces is shown, with a–c) a gray rectangle, indicating the time window in which the energy is integrated. (The time window starts at $\tau_0' + \tau_d$, with $\tau_0 \simeq 1202$ ps.), or d–f) the integrated time window around the echo. In d–f) the scheme on top represents the echo order.

ratio, and the signal is less affected by vapor absorption lines which are very strong at higher frequencies. Additionally, since the patterned logo features sub-millimeter details (e.g., the edges of the letters), lower frequencies would produce wavelengths too large to isolate the logo response from the combined response of the logo and the substrate.

Point measurements are shown in **Figure** 5a,d, whereas 2-D images are shown in Figure 5b,c,e–i. In Figure 5a,d, the amplitude reflection spectra of the open and the assembled tag, respectively, are taken at three different points (see the corresponding colored spots in Figure 5b,c,e,f) and compared. The advantage of this kind of analysis is the possibility to recognize the spectral fingerprint of the materials composing the multilayer and their THz characteristics. In particular, the results confirm the behavior of the THz radiation in the ceramic (refraction) and the metallic (reflection) areas, which causes the generation of multiple reflections in the substrates. This behavior is typical of a Fabry–Perot étalon, meaning that the signal resonates inside the Rogers layers at certain frequencies, predicted by its free spectral range (FSR).

For the open tag, this behavior is observed only outside the nonpatterned area, where the signal passes through the Rogers

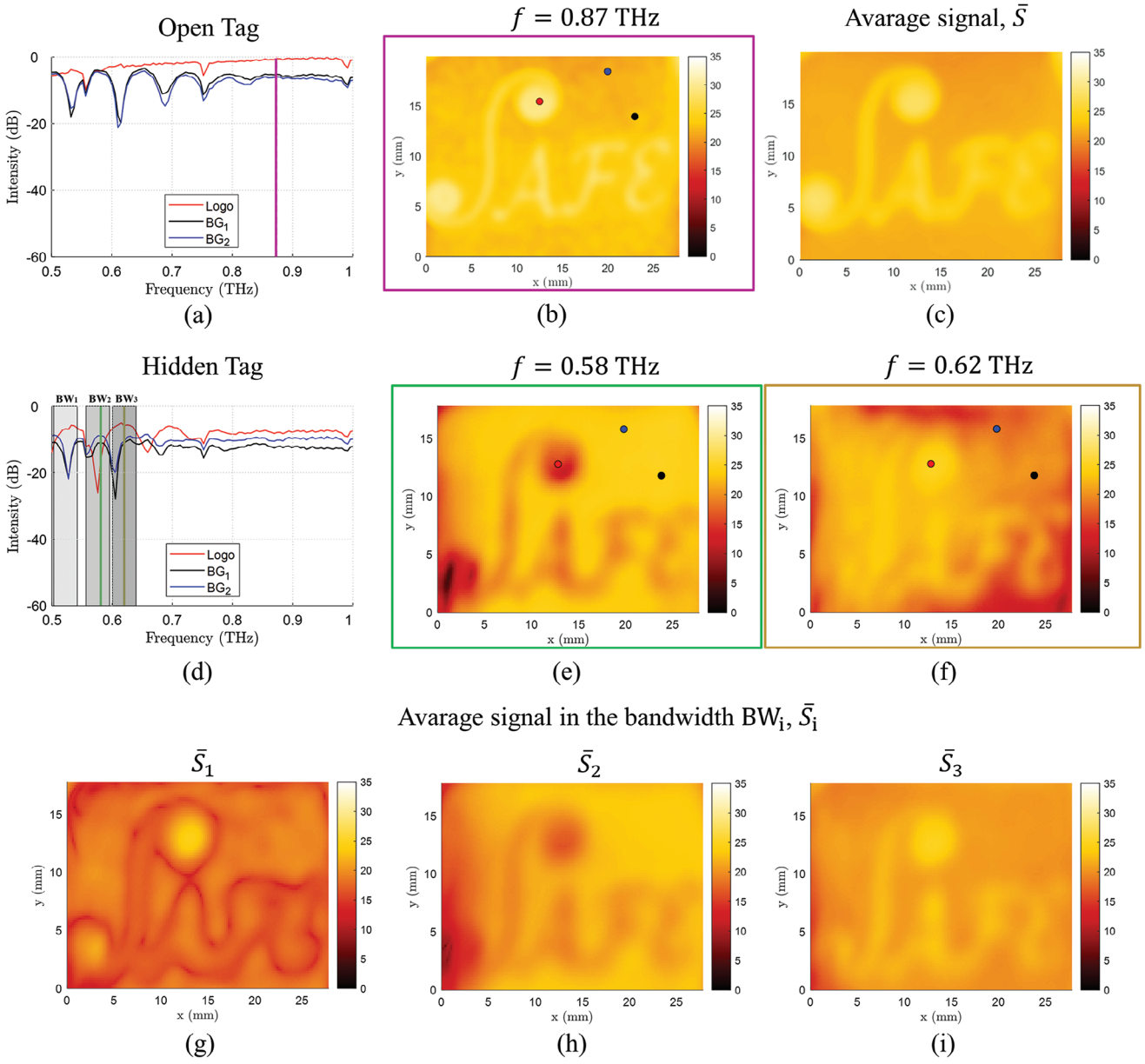

Figure 5. a) Spectra acquired from three points on the open tag. The red line is from a point on the logo, the black and blue lines are taken from the background. The purple line indicates the frequency $f = 0.87$ THz at which the frequency-domain image in b) is taken. In b),c), and e), the three indicated spots correspond to the measured pixels, whose spectra are reported in a) and d). c) Frequency-domain image obtained by averaging the signal in the entire frequency window. d) As in a), but for the assembled tag. The green and yellow lines indicate the frequency where the frequency-domain images are evaluated, namely at e) $f = 0.58$ THz and f) $f = 0.62$ THz. g–i) Frequency-domain image taken averaging the signal on the frequency windows g) BW_1 0.50–0.54 THz, h) BW_2 0.55–0.59 THz, i) BW_3 0.60–0.64 THz.

substrate before being reflected by the metal plate, thus the FSR reads

$$\mathrm{FSR}_{\mathrm{OT}} = \frac{c_0}{2d_\mathrm{s}\cos\theta_\mathrm{s} n_\mathrm{s}} \tag{8}$$

corresponding to ≈ 88 GHz. In contrast, the hidden tag is more complex. Around the logo, it can be described as a Fabry–Perot étalon similar to the nonpatterned area for the open tag, meaning they have a similar free spectral range $\mathrm{FSR}_{\mathrm{HT,\,logo}} \simeq \mathrm{FSR}_{\mathrm{OT}}$. However, outside the logo, the device comprises two ceramic substrates separated by an air gap whose thickness varies across pixels. In this case, the free spectral range reads

$$\mathrm{FSR}_{\mathrm{HT,\,bare}} = \frac{c_0}{2(2d_\mathrm{s}\cos\theta_\mathrm{s} n_\mathrm{s} + d_\mathrm{gap}\cos\theta_\mathrm{i})} \tag{9}$$

which ranges from 41 GHz, at the center of the sample where $d_\mathrm{gap} = 240\,\mu\mathrm{m}$ to 44 GHz at its edges where $d_\mathrm{gap} = 0\,\mu\mathrm{m}$. The air gap has a significant effect on the FSR. Without it, the logo

FSR would be exactly half that of the areas outside the logo, i.e., $FSR_{HT,\,bare} \simeq 2FSR_{OT}$ causing the resonances of the signal from the logo area to alternately overlap with those of the signal from the nonpatterned area. However, the presence of the air gap shifts and clearly distinguishes the signals.

Figure 5a shows the spectra taken at three different points of the open tag, two on the Rogers substrate and one on the "Safe" logo. The spectra from the substrate are mostly overlapped, even though they are from two pixels distant by a few millimeters apart, confirming the quasi-homogeneity of the substrate. They also demonstrate the dielectric behavior of the Rogers layer and its capability of acting as a Fabry–Perot étalon, whose measured FSR_{OT} is 81 GHz. We stress that the open logo is not metalized on the backside, but lies on the aluminum plate. Given its nearly flat surface, an air gap is to be expected, thus explaining the slight discrepancy with respect to the theoretically predicted FSR_{OT} (viz., 88 GHz). In contrast, the spectrum of the logo exhibits metallic behavior, with the signal completely reflected and only water absorption features being recognizable. The frequency-domain image obtained by assigning each pixel the signal intensity at a fixed frequency value $S(f)$ within the considered range highlights the high reflectivity of the "Safe" logo compared to the substrate. In Figure 5b the frequency-domain image at $f = 0.87$ THz (indicated by the magenta line in Figure 5a) is shown as an example, where the three dots represent the pixels from which the spectra in Figure 5a are taken. A similar result is achieved by averaging the signal over all the considered areas, with respect to the entire frequency range under analysis (viz., BW = [0.5, 1.0] THz), i.e., computing the following metrics

$$\bar{S} = \frac{1}{\Delta \mathrm{BW}} \int_{f \in \mathrm{BW}} |S(f)| \mathrm{d}f \tag{10}$$

where $\Delta \mathrm{BW} = \max \mathrm{BW} - \min \mathrm{BW}$. While inhomogeneities from both the substrate and the logo are smoothed out, no further information is extrapolated.

Figure 5d reveals that the spectra from the assembled tag are more complex, since the signal reflected from the hidden logo also passes through the dielectric material. Therefore, both the signal acquired from the "Safe" logo and from those areas outside of it exhibit a Fabry–Perot behavior. We emphasize that the FSR of the Fabry–Perot étalon differs in correspondence with the logo (only the first Rogers layer) and outside of it (both substrates and the air gap). Therefore, for the logo (measured in correspondence of the red dot in Figure 5e,f) $FSR_{HT,\,logo} = 88$ GHz, in excellent agreement with the theoretical value, whereas the spectra obtained from the two points outside the logo (black and blue dots in Figure 5e,f) have $FSR_{HT,\,bare}$41 GHz. We also note that the spectra for these two points (near the logo) are similar, confirming that the air gap is fairly homogeneous in this region.

Frequency-domain images generated at fixed frequencies do not present the same imaging contrast as in the case of the open tag. Figure 5e,f shows the Frequency-domain images acquired at $f = 0.58$ THz and 0.62 THz (green and orange lines in Figure 5d, respectively). The imaging contrast varies between the two images due to the combined Fabry–Perot behavior of the signals at the logo and outside of it. The reflectivity of these regions exhibits maxima at different positions, meaning that while in Figure 5e the response outside the logo dominates (cf., with the results of Figure 5d at 0.58 THz), in Figure 5f the logo reflectivity is higher (cf. with the results of Figure 5d at 0.62 THz). This effect repeats periodically.

As a result of the alternating behavior of the spectra from inside and outside the logo, the frequency-domain images obtained by averaging the reflectivity over the entire frequency window considered fail to show any information, rendering the logo indistinguishable from the background. However, the spectral analysis suggests that different metrics can be obtained by averaging the signal over narrower frequency bandwidths, namely $\mathrm{BW}_1 = [0.50, 0.54]$ THz, $\mathrm{BW}_2 = [0.55, 0.59]$ THz, and $\mathrm{BW}_3 = [0.60, 0.64]$ THz. This analysis naturally brings to the definition of the following metrics:

$$\bar{S}_i = \frac{1}{\Delta \mathrm{BW}_i} \int_{f \in \mathrm{BW}_i} |S(f)| \mathrm{d}f \tag{11}$$

with the obvious meaning of $\Delta \mathrm{BW}_i$ for $i = 1, 2, 3$. Figure 5g– i shows the frequency-domain images obtained by averaging the signal in the three frequency ranges indicated in the graph in Figure 5d, labeled as BW_i for $i = 1, 2, 3$ according to the definitions above. In particular, in the first case, the interference of signals from both the logo and its surroundings creates a contrast not achievable with the open logo, where only the "Safe" edges are distinguishable. This effect can only be observed if the frequency bandwidth is carefully selected. In fact, the imaging contrast on the edges is due to the difference between the maxima reflected by the logo and its surroundings. When these two values coincide, no contrast is visible. Conversely, when the integration occurs within windows where one of the two reflectivities prevails, one showing a maximum and the other a minimum, the former dominates the latter, resulting in complementary image contrasts as seen in Figure 5h,i.

5. Conclusion

We have demonstrated an efficient strategy for fabricating and characterizing hidden tags at THz frequencies. Our results highlight that commonly used techniques are effective for open tags, where the logo is optically visible, but they fail to detect tags embedded in multilayered materials, that are advantageous for integration into security and technological devices since they are undetectable by visible light or direct contact.

We have proposed an electromagnetic approach that considers the interaction of the THz radiation within dielectric and metallic materials and exploits the characteristics of the different raw spectra to create several metrics that, in this case, aim to define the best conditions for decoding the hidden tag.

In the time-domain raw spectra, we identified the best time windows for integrating the signal to maximize the imaging contrast. The highest resolution is obtained when the signal is integrated in a window of 4 ps, centered around the time at which the first-order reflection from the logo is collected.

In the frequency-domain analysis, instead, we focused on the difference between the electromagnetic response of the open and the assembled tag. In particular, the reflectivity from the hidden tag exhibits a Fabry–Perot behavior, meaning the imaging contrast changes periodically at different frequencies. Therefore,

integrating the signal over specific frequency windows can either maximize or smear out the contrast or, in some cases, highlight the tag edges, depending on the presence of maxima in the signal.

This analysis not only defines the best strategies for decoding hidden tags but is also relevant for designing anti-counterfeiting devices. In fact, both time- and frequency-domain results are heavily influenced by the tag design, including the number of layers, their thicknesses, refractive indices, and selected materials. By finely adjusting the device design, its THz response can be tuned as well, to ensure the logo is recognizable at different time windows or exhibits varying imaging contrasts at specific frequencies.

Our analysis points out that the metrics enabling tag recognition are intrinsically linked to physical phenomena arising from the interaction of the radiation with the stratified layers of materials, having different refractive indices at THz frequencies. This interaction generates multiple reflections within the multilayered device, which can be analyzed using their geometric optical paths (in the time domain) and their Fabry–Perot behavior (in the frequency domain). The primary contribution arises not from the specular reflection of individual materials but from the constructive and destructive interferences of multiple reflections, predominantly occurring within the air gap. As a result, this protocol is applicable to any stratified and multicomposite device, not necessarily limited to ceramic or metallic components, provided the THz radiation can penetrate the initial layer.

This customization enhances the security and uniqueness of the hidden tag, making it more challenging to counterfeit, as only by knowing all the specifics of the entire fabrication process of the device, its electromagnetic response can be predicted.

Acknowledgements

The work of T.R., D.C.Z., S.T., and R.B. was supported by the European Union, Next GenerationEU, through the project ECS00000024 "Ecosistemi dell'Innovazione"—Rome Technopole— CUP B83C22002890005 of the Italian Ministry of University and Research, public call n. 3277, PNRR-Mission 4, Component 2, Investment 1.5. The work of Walter Fuscaldo was supported by the European Union, Next GenerationEU, through the Project PRIN 2022 "Spiral and Focused Electromagnetic fields" (SAFE) of the Italian Ministry of University and Research (MUR), under Grant 2022ESAC3K.

Open access publishing facilitated by Consiglio Nazionale delle Ricerche, as part of the Wiley - CRUI-CARE agreement.

Conflict of Interest

The authors declare no conflict of interest.

Data Availability Statement

The data that support the findings of this study are available from the corresponding author upon reasonable request.

Keywords

anticounterfeiting devices, fabry–perot, terahertz imaging, terahertz time-domain spectroscopy

Received: October 26, 2024
Revised: December 6, 2024
Published online:

[1] L. Li, *Bus. Horiz.* **2013**, *56*, 167.
[2] S. P. Gayialis, E. P. Kechagias, G. A. Papadopoulos, D. Masouras, *Sustainability* **2022**, *14*, 6666.
[3] P. Aldhous, *Nature* **2005**, *434*, 7030.
[4] M. Pecht, S. Tiku, *IEEE Spectr.* **2006**, *43*, 37.
[5] C. Sheridan, *Nat. Biotechnol.* **2007**, *25*, 707.
[6] L. Ju, W. Gao, J. Zhang, T. Qin, Z. Du, L. Sheng, S. X.-A. Zhang, *J. Mater. Chem. C* **2020**, *8*, 2806.
[7] J. Liu, Y. Zhuang, L. Wang, T. Zhou, N. Hirosaki, R.-J. Xie, *ACS Appl. Mater. Interfaces* **2018**, *10*, 1802.
[8] M. D. L. Bruno, G. E. Lio, A. Ferraro, S. Nocentini, G. Papuzzo, A. Forestiero, G. Desiderio, M. P. De Santo, D. S. Wiersma, R. Caputo, G. Golemme, F. Riboli, R. C. Barberi, *ACS Appl. Mater. Interfaces* **2024**, *16*, 37063.
[9] S. Ren, B. Liu, M. Wang, G. Han, H. Zhao, Y. Zhang, *J. Mater. Chem. C* **2022**, *10*, 11338.
[10] F. Zhang, Z. Shi, S. Li, Z. Ma, Y. Li, L. Wang, D. Wu, Y. Tian, G. Du, X. Li, C. Shan, *ACS Appl. Mater. Interfaces* **2019**, *11*, 28013.
[11] L. Zhu, D. Shen, Q. Wang, K. H. Luo, *ACS Appl. Mater. Interfaces* **2021**,*13*, 56465.
[12] T. Ritacco, G. E. Lio, X. Xu, A. Broussier, A. Issa, M. Giocondo, R. Bachelot, S. Blaize, C. Couteau, S. Jradi, *ACS Appl. Nano Mater.* **2021**, *4*, 6916.
[13] W. Ren, G. Lin, C. Clarke, J. Zhou, D. Jin, *Adv. Mater.* **2020**, *32*, 1901430.
[14] A. Abdollahi, H. Roghani-Mamaqani, B. Razavi, M. Salami-Kalajahi, *ACS Nano* **2020**, *14*, 14417.
[15] Y. Shi, J. Han, X. Jin, W. Miao, Y. Zhang, P. Duan, *Adv. Sci.* **2022**, *9*, 2201565.
[16] M. D. L. Bruno, E. Fuoco, G. Petriashvili, G. Papuzzo, A. Forestiero, S. Sinopoli, U. Emanuele, R. C. Barberi, M. P. De Santo, *Adv. Mater. Technol.* **2023**, *8*, 2300613.
[17] T. Ritacco, D. M. Aceti, G. De Domenico, M. Giocondo, A. Mazzulla, G. Cipparrone, P. Pagliusi, *Adv. Opt. Mater.* **2022**, *10*, 2101526.
[18] T. Ritacco, A. Mazzulla, R. Beccherelli, P. Pagliusi, *Liq. Cryst.* **2024**, 1.
[19] W. Hong, Z. Yuan, X. Chen, *Small* **2020**, *16*, 1907626.
[20] J. Wang, J. Ma, J. Zhang, Y. Fan, W. Wang, J. Sang, Z. Ma, H. Li, *ACS Appl. Mater. Interfaces* **2019**, *11*, 35871.
[21] S. Nocentini, U. Rührmair, M. Barni, D. S. Wiersma, F. Riboli, *Nat. Mater.* **2024**, *23*, 369.
[22] M. J. Aitken, *Thermoluminescence Dating*, Academic Press, London, UK **1985**.
[23] A. Cosentino, *Technologies* **2016**, *4*, 6.
[24] A. Gibson, K. E. Piquette, U. Bergmann, W. Christens-Barry, G. Davis, M. Endrizzi, S. Fan, S. Farsiu, A. Fitzgerald, J. Griffiths, C. Jones, G. Li, P. L. Manning, C. Maughan Jones, R. Mazza, D. Mills, P. Modregger, P. R. T. Munro, A. Olivo, A. Stevenson, B. Venugopal, V. Wallace, R. A. Wogelius, M. B. Toth, M. Terras, *Herit. Sci.* **2018**, *6*, 1.
[25] E. Abraham, K. Fukunaga, *Stud. Conserv.* **2015**, *60*, 343.
[26] Z. Yan, L.-G. Zhu, K. Meng, W. Huang, Q. Shi, *Trends Biotechnol.* **2022**, *40*, 816.
[27] Z. D. Taylor, R. S. Singh, D. B. Bennett, P. Tewari, C. P. Kealey, N. Bajwa, M. O. Culjat, A. Stojadinovic, H. Lee, J.-P. Hubschman, E. R. Brown, W. S. Grundfest, *IEEE Trans. THz Sci. Technol.* **2011**, *1*, 201.
[28] M. Gezimati, G. Singh, *IEEE Access* **2023**, *11*, 18590.
[29] A. Sadeghi, S. M. H. Naghavi, M. Mozafari, E. Afshari, *Trans. Oncol.* **2023**, *27*, 101565.

[30] J. B. Jackson, J. Bowen, G. Walker, J. Labaune, G. Mourou, M. Menu, K. Fukunaga, *IEEE Trans. THz Sci. Technol.* **2011**, *1*, 220.
[31] C. Seco-Martorell, V. López-Domínguez, G. Arauz-Garofalo, A. Redo-Sanchez, J. Palacios, J. Tejada, *Opt. Express* **2013**, *21*, 17800.
[32] K. Fukunaga, *THz Technology Applied to Cultural Heritage in Practice*, Springer, Berlin **2016**.
[33] K. Fukunaga, *Heritage* **2023**, *6*, 3448.
[34] M. Flammini, C. Bonsi, C. Ciano, V. Giliberti, E. Pontecorvo, P. Italia, E. DelRe, M. Ortolani, *J. Infra. Millim. Terahz Waves* **2017**, *38*, 435.
[35] R. Manca, L. Chiarantini, E. Tartaglia, F. Soldovieri, C. Miliani, I. Catapano, *Coatings* **2023**, *13*, 1268.
[36] A. A. Gowen, C. O'Sullivan, C. P. O'Donnell, *Trends Food Sci. Technol.* **2012**, *25*, 40.
[37] S. Wietzke, C. Jördens, N. Krumbholz, B. Baudrit, M. Bastian, M. Koch, *J. Eur. Opt. Soc.-Rapid* **2007**, *2*, 07013.
[38] K. Ahi, S. Shahbazmohamadi, N. Asadizanjani, *Opt. Lasers Eng.* **2018**, *104*, 274.
[39] L. Afsah-Hejri, P. Hajeb, P. Ara, R. J. Ehsani, *Compr. Rev. Food Sci. Food Saf.* **2019**, *18*, 1563.
[40] S. Zappia, R. Scapaticci, M. B. Lodi, A. Fanti, G. Ruello, L. Crocco, I. Catapano, *IEEE Trans. THz Sci. Technol.* **2023**, *13*, 305.
[41] G. Ren, Z. Zhu, J. Zhang, H. Zhao, Y. Li, J. Han, *Opt. Commun.* **2020**, *475*, 126267.
[42] H. J. Shin, M.-C. Lim, K. Park, S.-H. Kim, S.-W. Choi, G. Ok, *Sensors* **2017**, *17*, 2825.
[43] P. Hoveida, A. Phoulady, H. Choi, N. May, S. Shahbazmohamadi, P. Tavousi, *Sci. Rep.* **2023**, *13*, 12474.
[44] S. Kamwe Sighano, T. Ritacco, M. D. L. Bruno, O. Gennari, W. Fuscaldo, D. C. Zografopoulos, J. Marae-Djouda, T. Maurer, R. Beccherelli, R. Caputo, A. Ferraro, *Adv. Funct. Mater.* **2024**, *34*, 2406632.
[45] D. M. Mittleman, *Opt. Express* **2018**, *26*, 9417.
[46] J. Dong, A. Locquet, M. Melis, D. Citrin, *Sci. Rep.* **2017**, *7*, 15098.
[47] J. Dong, J. Bianca Jackson, M. Melis, D. Giovanacci, G. C. Walker, A. Locquet, J. W. Bowen, D. S. Citrin, *Opt. Express* **2016**, *24*, 26972.
[48] J. Dong, X. Wu, A. Locquet, D. S. Citrin, *IEEE Trans. THz Sci. Technol.* **2017**, *7*, 260.
[49] J. L. M. Van Mechelen, A. B. Kuzmenko, H. Merbold, *Optics Lett.* **2014**, *39*, 3853.
[50] M. Zhai, D. Citrin, A. Locquet, *J. Infra. Millim. Terahz Waves* **2021**, *42*, 929.
[51] A. Moradikouchi, A. Sparén, S. Folestad, J. Stake, H. Rodilla, *Int. J. Pharm.* **2022**, *618*, 121579.
[52] W. Fuscaldo, S. D. Simone, D. Dimitrov, V. Marinova, V. Mussi, R. Beccherelli, D. C. Zografopoulos, *J. Phys. D: Appl. Phys.* **2022**, *55*, 365101.
[53] S. Tofani, T. Ritacco, L. Maiolo, F. Maita, R. Beccherelli, W. Fuscaldo, D. C. Zografopoulos, *Crystals* **2024**, *14*, 205.
[54] Toptica Photonics, https://www.toptica.com/products/terahertz-systems/ (accessed: december 2024).